Amplification of turbulent exchange over wide Arctic leads: Large-eddy simulation study

I. N. Esau[1]

Received 24 February 2006; revised 23 August 2006; accepted 12 September 2006; published 26 April 2007.

[1] Leads (narrow openings in the sea ice cover) are perhaps the most pronounced examples of heat islands naturally occurring on Earth. Large air-water temperature differences induce strong turbulent convection. In addition, large ice-water temperature differences induce more regular, breeze-like circulation at ice edges. Both the turbulent convection and the breeze result in intensive turbulent heat exchange between the ocean and the atmosphere. This study describes a series of turbulence-resolving experiments with the Large Eddy Simulation Nansen Center Improved Code (LESNIC). The numerical experiments quantify the turbulent heat exchange over leads of different widths. Contrary to the expected gradual decrease of the surface heat flux per unit area of open water, a strong amplification of the heat flux has been discovered for certain leads. This amplification results from a positive feedback between the horizontal entrainment of cool air in breeze and the turbulent heat exchange. Gradual reduction of the turbulent exchange for wider leads is thought to be due to development of self-organized structures in the convection. Pressure anomalies induced by the convective overturning could be comparable with the pressure anomalies due to the surface temperature difference. Their superposition limits the penetration of the cold breeze into the lead area. Without the horizontal entrainment, the near-surface temperature rises, reducing the average turbulent fluxes. In addition, the structures use the available kinetic energy to drive convective overturning. It also reduces the near-surface velocity and therefore fluxes. The maximum heat flux over open water was obtained for 2 km to 4 km leads. The maximum flux exceeds five-fold the flux in the homogeneous convection case. The revealed flux enhancement may have significant impact on the Arctic climate and more generally on the climate of urban areas and other heat islands. Therefore direct confirmation of the results from observational campaigns is urgently needed.

Citation: Esau, I. N. (2007), Amplification of turbulent exchange over wide Arctic leads: Large-eddy simulation study, *J. Geophys. Res.*, *112*, D08109, doi:10.1029/2006JD007225.

1. Introduction

[2] Leads (narrow (1 m to 10^4 m) openings in the Arctic Ocean ice cover with length up to several hundreds kilometres) are the major source of heat and moisture in the atmosphere over the central Arctic Ocean. The leads cover 1% to 5% of the central Arctic [*Miles and Barry*, 1998] and up to 20% of the Arctic marginal seas [*Lindsay and Rothrock*, 1995; *Inoue et al.*, 2005]. Their importance is disproportional to their area coverage. In situ studies suggest [e.g., *Makshtas*, 1991; *Eisen and Kottmeier*, 2000] that leads could be responsible for up to 80% of the observed turbulent mixing in polar areas. Aircraft measurements during field campaigns, e.g., BASE [*Paluch et al.*, 1997], REFLEX [*Hartmann et al.*, 1994] and LEADEX [*Walter et al.*, 1995; *Ruffieux et al.*, 1995], obtained an average turbulent heat flux over open water as large as 50 W m^{-2} in strong, up to 16 m s^{-1}, wind conditions. In some cases the flux could reach 150 W m^{-2} [e.g., *Inoue et al.*, 2005] and even larger values [*Andreas and Cash*, 1999]. Thin ice cover reduces the flux to just a few W m^{-2}, e.g., the downward sensible heat flux over ice did not exceed 2 W m^{-2} during BASE.

[3] The lead width is considered to be an important parameter in determination of the heat flux over open water [e.g., *Maslanik and Key*, 1995]. *Andreas and Murphy* [1986] and *Serreze et al.* [1992] argued that the turbulent heat flux from the unit area of the open water surface, H_s, is larger over narrow leads and during weak wind episodes because of abrupt change in the surface temperature at the ice-water edge. Their conceptual model suggests a nonlinear but monotonic decrease of the lead-induced temperature flux $F_s = H_s/(\rho\, c_p)$ at the surface and a monotonic increase of the mean mixed layer depth h_{CBL} with increase of the lead width, λ. Here ρ is the air density and c_p is the air specific heat under constant pressure. Simple bulk models [*Maslanik and Key*, 1995], an internal boundary layer model driven by sounding data [*Serreze et al.*, 1992] and more

[1]Nansen Environmental and Remote Sensing Center, Bergen, Norway.

0148-0227/07/2006JD007225

sophisticated single-column models [*Alam and Curry*, 1997; *Renfrew and King*, 2000] reproduced the empirical behavior of $F_s(\lambda)$ over narrow leads. On the basis of this success the models extrapolate the monotonic dependence to wider, kilometer-scale leads.

[4] *Barry et al.* [1989] and *Lindsay and Rothrock* [1995] statistics indicates that the leads wider than 1 km constitute about 30% of the total number of leads and cracks detected in aircraft Lidar data. They expose to the atmosphere the major fraction of the open water surface in the Arctic Ocean. Statistics show the mean lead width between 2 km and 4 km in the central Arctic and 4 km to 6 km in peripheral seas. The mean ice floe size is much larger than the mean lead width. It varies from 20 km in peripheral seas to 40 km in the central Arctic. These values motivate the interest to study turbulent exchange over wider 1 km to 10 km leads.

[5] With the absence of suitable field data, turbulence-resolving large-eddy simulations (LES) are the most convenient tool to assess validity of the monotonic extrapolation of the turbulent fluxes from meter to kilometer-scale leads. Results from earlier LES studies suggested a different, nonmonotonic behavior of $F_s(\lambda)$ over kilometer-scale surface heterogeneities. For instance simulations by *Shen and Leclerc* [1995], *Avissar and Schmidt* [1998], *Raasch and Harbusch* [2001] and *Letzel and Raasch* [2003] revealed that the kinetic energy of the induced secondary circulations could be much larger than the turbulent kinetic energy (TKE) of the convection. Moreover, the circulations have developed the strongest flow in the close proximity of the warmer surface. This founding indicated a possibility for additional heat exchange over large leads. The additional heat flux could not be discovered in the mentioned LES as they run with the prescribed $F_s(\lambda)$, where λ is a length scale of the surface heterogeneity. Recently, *Patton et al.* [2005], hereafter P05, has published a LES study of convection over dry-wet strip surface heterogeneity. In this study, the constant surface temperature and spatial variations of the surface moisture were prescribed. These model conditions allowed for variations of $F_s(\lambda)$, which could respond to the development of secondary circulations. The moisture variations were able to produce only modest changes in the surface temperature flux. Nevertheless, P05 found considerable, up to 20%, enhancement of the fluxes for kilometer-scale surface heterogeneity.

[6] The P05 study confirmed that $F_s(\lambda)$ is a nonmonotonic function of the surface temperature heterogeneity length scale. With just six LES runs, details of the nonmonotonic flux behavior remained uncertain in this study. *Avissar and Schmidt* [1998] and *Letzel and Raasch* [2003] noticed strong enhancement of the secondary circulations with increase of the amplitude of the surface temperature difference. It suggests that for Arctic leads, where the ice-water temperature difference could be as large as 30 K [*Andreas and Cash*, 1999], the secondary circulations and related surface flux enhancement could be very significant. Using two-dimensional model, *Zulauf and Krueger* [2003] found that $F_s(\lambda)$ follows the prediction from simplified models only for $\lambda < 500$ m in the case without geostrophic wind, $U_g = 0$ m s^{-1}. For wider leads $\lambda > 500$, $F_s(\lambda)$ was increasing. In the case with a significant mean cross-lead wind, $U_g = 2.5$ m s^{-1}, F as also decreasing over wider, up to $\lambda \approx 1600$ m, leads. The cases with nonzero U_g will not be considered in this work. Nevertheless, it is worth to mention that the importance of the mean cross-lead wind depends on its speed relative to the wind speed of the secondary circulation and convective eddies [e.g., *Avissar and Schmidt*, 1998]. Since wider leads and larger surface temperature differences induce stronger circulations, the weak and even moderate mean winds ($U_g = 7.5$ m s^{-1} by *Raasch and Harbusch* [2001]) may not totally smooth the nonmonotonic behavior of $F_s(\lambda)$ over the Arctic leads.

[7] Even without the mean wind, lead-induced circulation is a complex phenomenon combining turbulent convection and more regular breeze-like circulation. Low wind conditions are frequently observed in Arctic. For instance during the 1997–1998 SHEBA campaign [*Uttal et al.*, 2002], a wind speed less than 2 m s^{-1} was observed during 60 days as follows from my analysis of 255 days of SHEBA data. The data was obtained from http://www.joss.ucar.edu/sheba/index.html. Moreover, leads tend to align with the geostrophic wind direction [*Barry et al.*, 1989]. In this case, the cross-lead component of the wind should be dominated by the lead-induced circulation. P05 suggests that the convection-breeze interaction should result in the enhanced temperature flux at scales from 2 km to 5 km. These scales coincide with the mean lead widths [*Lindsay and Rothrock*, 1995]. Thus it is reasonable to expect significant contribution of kilometer-scale leads in the total heat budget of the Arctic.

[8] Here, new LES provide details of the turbulent mixing over leads from a few meters to about ten kilometers in width. Section 2 describes the Large Eddy Simulation Nansen Center Improved Code (LESNIC), initial and boundary conditions and setup of numerical experiments. Section 3 provides definitions for derived quantities and model sensitivity analysis. Section 4 presents simulation results. Section 5 discusses physical mechanisms. Section 6 highlights conclusions.

2. Turbulence-Resolving Model

2.1. Large-Eddy Simulation Code LESNIC

[9] The study relies on ability of a three-dimensional turbulence-resolving LES code to generate fluctuating velocity and temperature fields consistent with simple boundary conditions. Being verified in case studies, LES statistics derived from these fluctuations are able to compensate a lack of direct field data for research. A series of numerical experiments was conducted with the large-eddy simulation code LESNIC. *Esau* [2004] describes the code and its validation against homogeneous, steady state turbulence statistics in the Ekman boundary layer. *Fedorovich et al.* [2004] and *Zilitinkevich et al.* [2006] compared the LESNIC output with the data for the atmospheric forced and free convection. *Esau and Zilitinkevich* [2006] compared the code performance at different model resolutions. *Beare et al.* [2006] described the intercomparison of 11 LES codes including the NERSC code LESNIC. The main advantage of the LESNIC code is its ability to simulate stratified boundary layers without manual tuning of model parameters. This advantage results from implementation of a dynamic mixed turbulence closure in the model. The HATS atmospheric data [*Sullivan et al.*, 2003; *Kleissl*

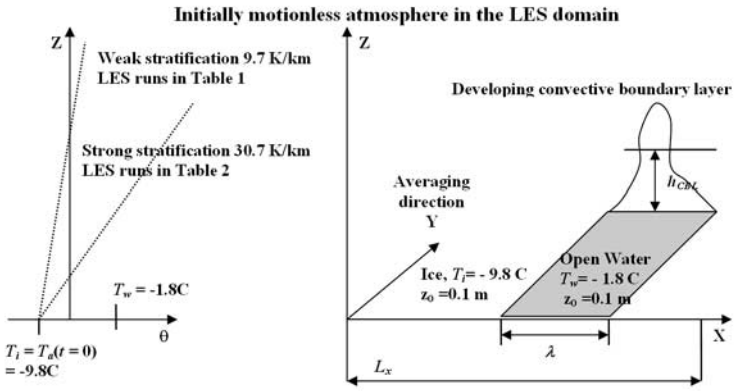

Figure 1. Schematic diagram of initial and boundary conditions of the Large Eddy Simulation (LES) runs.

et al., 2003] confirms the necessity of such an approach for turbulence-resolving simulations of the atmospheric boundary layers.

[10] The LESNIC solves the momentum, temperature and continuity equations for incompressible Boussinesq fluid in the following form:

$$\frac{\partial u_i}{\partial t} = -\frac{1}{2}u_j\frac{\partial u_i}{\partial x_j} - \frac{\partial}{\partial x_j}\left(\frac{1}{2}u_iu_j + p\delta_{ij} + \tau_{ij}\right) - f\omega_j - g\beta\theta\delta_{i3}, \quad (1)$$

$$\frac{\partial \theta}{\partial t} = -\frac{\partial}{\partial x_j}\left(u_j\theta + \tau_{\Theta j}\right), \frac{\partial u_i}{\partial x_i} = 0 \quad (2)$$

Here $u_i = \{u,v,w\}$, $\theta = \mathrm{T}(1000/\mathrm{p})^{0.287}$ are the resolved-scale velocity and potential temperature; T is the absolute temperature; p is the pressure; τ_{ij}, $\tau_{\Theta j}$ are the subgrid-scale turbulence stress and diffusivity tensors to be modelled with the dynamic mixed subgrid closure [*Vreman et al.*, 1994]; $\beta = 0.003\mathrm{K}^{-1}$ is the thermal expansion coefficient; g = 9.81 m s^{-1} is the acceleration due to gravity; $f\omega_j = \{f(v_g - v + w \cdot \cot\varphi), f(-u_g + u), f(-u\cot\varphi)\}$ are the components of the Coriolis force; $f = 2\Omega\sin\varphi$ is the Coriolis parameter; φ is the latitude; $\Omega = 7.27\ 10^{-5}$ s^{-1} is the Earth's angular velocity; $\delta_{ij} = 1$ for $i = j$ and $\delta_{ij} = 0$ for $i \neq j$; the repeating indexes imply summation.

[11] The LESNIC employs a fully conservative second-order central difference scheme for advection, the fourth-order Runge-Kutta scheme for time stepping, and a direct fractional step pressure correction scheme to solve the continuity equation. The computational mesh is an equidistant, staggered C-type mesh. The dynamic mixed closure models the subgrid terms as

$$\tau_{ij} = L_{ij} - 2l_s^2|S_{ij}|S_{ij}, \quad \tau_{\Theta j} = -2\mathrm{Pr}_t^{-1}l_s^2|S_{ij}|\frac{\partial\theta}{\partial x_j}, \quad (3a)$$

where Pr_t is an empirical turbulent Prandtl number taken after *Kondo et al.* [1978]. The model requires only normal component of turbulent fluxes at the surface as the bottom boundary conditions. However, the surface temperature has been prescribed in the set of experiments. I used simplified formulation describing the near-neutral logarithmic layer as

$$\tau_{i3}(z=0) = C_{DN}u_i(\mathrm{z}_1)\cdot|\vec{u}(\mathrm{z}_1)|,$$
$$\tau_{\Theta;3}(z=0) = C_{DH}\left(\theta(z_1) - T_{i,w}\right)|\vec{u}(z_1)|. \quad (3b)$$

Here, $C_{DN} = C_{DH} = (0.41/\ln(z/z_0))^2$ are the neutral transfer coefficients, z_0 is the surface roughness, z_1 is the height of the first computational level in the model and $\mathrm{T}_{i,w}$ is the absolute surface temperature for ice and water respectively.

[12] A mixing length scale $l_s(x_i,t)$ is computed at every grid node and at every time step through a numerical solution of a deconvolution problem for filtered (grid-scale) velocities using the least square minimization method [*Vreman et al.*, 1994]. The resulting algebraic equation is

$$l_s^2 = \frac{\Delta^2}{2}\frac{\left(L_{ij} - H_{ij}\right)\cdot M_{ij}}{M_{ij}\cdot M_{ij}}, \quad (4)$$

where resolved-scale tensors L_{ij}, H_{ij}, M_{ij} and S_{ij} are defined using two spatial Gaussian filters denoted by angular brackets for the grid-scale filter and by overbars for larger, twice grid-scale filter. The expressions are

$$S_{ij} = \frac{1}{2}\left(\frac{\partial u_i}{\partial x_j} + \frac{\partial u_j}{\partial x_i}\right), L_{ij} = \overline{(u_iu_j)} - \overline{u_i}\,\overline{u_j}, \quad (5)$$

$$M_{ij} = \overline{\left(|S_{ij}|S_{ij}\right)} - \alpha^2|\overline{S_{ij}}|\overline{S_{ij}}, \quad (6)$$

$$H_{ij} = \overline{\left(\langle\overline{u_i}\,\overline{u_j}\rangle\right)} - \overline{\langle\overline{u_i}\rangle\langle\overline{u_j}\rangle} - \left(\overline{\langle u_i\rangle\langle u_j\rangle} - \overline{\left(\langle u_i\rangle\langle u_j\rangle\right)}\right), \quad (7)$$

where $\alpha = 2.92$. To avoid numerical instability, l_s was limited to $l_s \in [0;1]\Delta$ where Δ is the geometrical mean grid size. This is not a restrictive limitation as the theory [*Leslie and Quarini*, 1979] predicts $l_s \in [0.16;0.23]\Delta$ in the homogeneous turbulence, while l_s should be smaller for the sheared turbulence. The complicated formulation in equations (4)–(7) seems to be important for high-quality simulations [*Sullivan et al.*, 2003; *Beare et al.*, 2006].

Table 1. External and Inferred Parameters after 6 hours of Integration for the Numerical Experiments With Initial Atmospheric Stability $\nabla_z\theta = 9.7$ K km^{-1}[a]

Run	Domain Size, m $L_x \times L_y \times L_z$	Mesh Size, m $\Delta_x \times \Delta_y \times \Delta_z$	Lead Width, m λ	$F_s \cdot 10^3$, K ms^{-1}	h_{CBL}, m
1	1024 × 32 × 48	1 × 1 × 1	5	14	21
2	1024 × 32 × 48	1 × 1 × 1	6	14	26
3	1024 × 32 × 48	1 × 1 × 1	7	16	30
4	1024 × 32 × 48	1 × 1 × 1	8	17	32
5	1024 × 32 × 48	1 × 1 × 1	9	23	36
6	1024 × 32 × 48	1 × 1 × 1	10	23	33
7	1024 × 32 × 48	1 × 1 × 1	11	26	40
8	3072 × 96 × 144	3 × 3 × 3	33	20	38
9	4096 × 128 × 144	4 × 4 × 3	44	24	53
10	3072 × 96 × 144	3 × 3 × 3	54	26	50
11	10240 × 320 × 144	10 × 10 × 3	60	33	38
12	10240 × 320 × 240	10 × 10 × 5	60	27	33
13	10240 × 320 × 240	10 × 10 × 5	80	29	38
14	20480 × 640 × 240	20 × 20 × 5	100	36	43
15	20480 × 640 × 240	20 × 20 × 10	160	33	35
16	20480 × 640 × 480	20 × 20 × 10	220	37	45
17	40960 × 640 × 480	20 × 20 × 10	220	32	55
18	20480 × 640 × 480	20 × 20 × 10	260	41	55
19	20480 × 640 × 480	20 × 20 × 10	300	38	65
20	20480 × 640 × 480	20 × 20 × 10	420	49	65
21	20480 × 640 × 480	20 × 20 × 10	620	64	105
22	20480 × 640 × 480	20 × 20 × 10	620	62	95
23	20480 × 640 × 480	20 × 20 × 10	620	63	95
24	20480 × 640 × 480	20 × 20 × 10	820	64	115
25	20480 × 640 × 480	20 × 20 × 10	1020	84	115
26	20480 × 640 × 480	20 × 20 × 10	1420	95	165
27	20480 × 640 × 480	20 × 20 × 10	1620	95	165
28	10240 × 320 × 480	10 × 10 × 10	2410	89	285
29	20480 × 640 × 480	20 × 20 × 10	2420	105	205
30[b,c]	20480 × 640 × 480	20 × 20 × 10	2420	101	245
31	20480 × 640 × 960	20 × 20 × 20	2420	80	190
32	10240 × 640 × 480	20 × 20 × 10	2420	73	275
33	40960 × 640 × 480	20 × 20 × 10	2420	134	205
34	20480 × 640 × 480	20 × 20 × 10	3220	98	255
35	20480 × 640 × 480	20 × 20 × 10	4820	92	295
36	40960 × 640 × 480	20 × 20 × 10	6440	99	275
37	20480 × 640 × 480	20 × 20 × 10	6420	74	285
38	20480 × 640 × 480	20 × 20 × 10	7020	67	295
39[c]	20480 × 640 × 480	20 × 20 × 10	7020	66	305
40	20480 × 640 × 480	20 × 20 × 10	9620	49	305
41	20480 × 640 × 480	20 × 20 × 10	12800	38	295
42	40960 × 640 × 480	20 × 20 × 10	12800	57	275
43[d]	20480 × 640 × 480	20 × 20 × 10	20480	19	265

[a]External parameters are given in columns 1–4; inferred parameters are given in columns 5 and 6.
[b]Run integrated for 12 model hours.
[c]Run computed for the latitude 80 degrees N.
[d]Run with the shear-free convection over a homogenous surface with the surface temperature fixed at −1.8 C.

2.2. Numerical Experiments

[13] Two series of 43 and 9 high-resolution numerical experiments have been conducted with the LESNIC code. Table 1 presents the experiments conducted with initial atmospheric stabilities $\nabla_z\theta = 9.7$ K km^{-1}. Table 2 presents the experiments with $\nabla_z\ \theta = 30.7$ K km^{-1}. Figure 1 sketches the initial setup of experiments. All experiments start from initially motionless, homogeneous, stably stratified boundary layers perturbed with temperature fluctuations of 0.1 K at the five lowest model levels over leads.

Table 2. Same Quantities as in Table 1 but for the Numerical Experiments With Initial Atmospheric Stability $\nabla_z\theta = 30.7$ K km^{-1}

Run	Domain Size, m $L_x \times L_y \times L_z$	Mesh Size, m $\Delta_x \times \Delta_y \times \Delta_z$	Lead Width, m λ	$F_s \cdot 10^3$, K ms^{-1}	h_{CBL}, m
44	768 × 96 × 48	3 × 3 × 1	21	6	20
45	1280 × 160 × 96	5 × 5 × 2	85	10	33
46	8192 × 320 × 192	8 × 10 × 4	208	14	10
47	8192 × 320 × 192	8 × 10 × 4	408	15	50
48	12288 × 384 × 288	12 × 12 × 6	804	19	45
49	12288 × 384 × 288	12 × 12 × 6	1608	31	75
50	12288 × 384 × 288	12 × 12 × 6	3852	22	90
51	15360 × 480 × 240	15 × 15 × 5	6405	13	92
52[a]	10240 × 320 × 192	10 × 10 × 4	10240	6	74

[a]Run with the shear-free c n over a homogenous surface with the surface temperature fixed at −1.8 C.

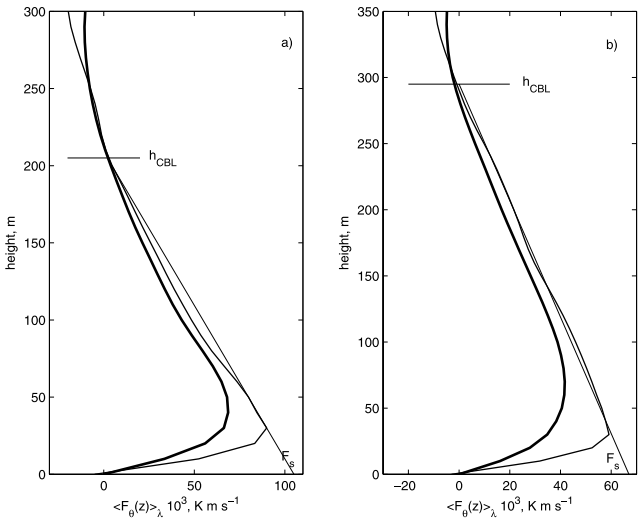

Figure 2. Definitions of the resolved-scale surface temperature flux per unit area of the open water F_s after equation (9) and the mean convective layers' depth h_{CBL}. Both quantities are computed from the resolved-scale temperature flux profile averaged over the open water area. Thin curves show instant fluxes for runs 29 (a) and 38 (b). Thick curves show the flux averaged over 1 hour with sampling interval 10 min.

[14] A lead is defined as a strip aligned with y direction. The lead surface temperature $T_w = -1.8$ C is a typical water freezing temperature in the Arctic Ocean. Ice surface temperature was taken $T_i = -9.8$ C. The ice temperature is often much lower in the Arctic. The moderate surface temperature difference of 8 K was taken to preserve the model stability and accuracy. The location of open water and ice surfaces and their temperatures do not change during the simulations. The surface roughness was $z_0 = 0.01$ m for open water and $z_0 = 0.1$ m for ice. Since the neutral transfer coefficients for momentum and temperature are prescribed, the direct comparison between the model results and the famous heat transfer coefficient dependence $C_{DN}(\lambda/L) = 10^{-3}(1 + 0.8\exp(0.05\lambda/L))$ by *Andreas and Murphy* [1986] is not possible. The latter dependence was obtained empirically for narrow leads with $\lambda < 200$ m. Here, $L = -|\tau_{i3}(z=0)|^{3/2}/(g\beta\,\tau_{\Theta 3}(z=0))$ is the Monin-Obukhov length scale. The upper boundary conditions prescribe a stress-free rigid lid, i.e., $\nabla_z u_i = \nabla_z \Theta = \nabla_z p = 0$, $w = 0$. The following discussion addresses LES runs from the Table 1 if there are no special remarks.

3. Definitions and Sensitivity Analysis

3.1. Resolved Surface Temperature Flux and Convective Layer Depth Definitions

[15] The central quantity in this study is the mean surface turbulent temperature flux over unit area of open water. This flux, $F_s(\lambda)$, gives efficiency of heat extraction from the upper ocean layer, thus being of the central interest for climatological studies. The value $F_s(\lambda)$ cannot be directly estimated from the large-eddy simulations as the turbulent exchange between the surface and the first computational level is parameterized the constant neutral exchange coefficients. The parameterized surface temperature flux, $\tau_\theta 3(z = 0)$, depends significantly on the specific parameterization method and will not be discussed here.

[16] The following analysis is focused on the resolved flux. One can use well established linear mean flux-height dependence for the case of the shear-free convection (e.g., BOMEX data by *Siebesma et al.* [2003]). It reads

$$\langle F_\theta(z)\rangle = (1 - z/h_{CBL})\langle F_s\rangle, \tag{8}$$

where $\langle\cdot\rangle$ denotes spatial averaging, z is the height above the surface; F_s is the surface temperature flux; and h_{CBL} is the mean depth of the convection layer over the lead. Equation (8) defines F_s and h_{CBL}. Figure 2 shows the temperature fluxes over the open water for runs 29 and 38. Obviously, the resolved flux satisfies equation (8) only above the surface layer, $z > 0.1h_{CBL}$. The flux reduction within the surface layer is caused by the shift of the spectral maximum of the turbulent kinetic energy (TKE) to unresolved length scales. Using the resolved fluctuations of the vertical component of velocity w' and potential temperature θ', the mean resolved flux becomes $\langle F_\theta(z)\rangle_\lambda = \langle w'\theta'\rangle_\lambda$ where $\langle\cdot\rangle_\lambda$ denotes averaging over the open water area. The convective layer depth is defined as the lowest height where $\langle F_\theta(z)\rangle_\lambda = 0$. Then the resolved surface flux is

$$F_s(\lambda) = \frac{\max\limits_{z\in[0,h_{CBL}]}\left(\langle F_\theta(z)\rangle_\lambda\right)}{1 - z^{\max}/h_{CBL}} \tag{9}$$

where $z^{\max}$ is the height of the maximum of $\langle F_\theta(z)\rangle$, and the notation $F_s = \langle F_s\rangle_\lambda$ is used for brevity. Figure 3 shows that the definition in equation (9) is in good correspondence with true surface fluxes, $\tau_{\theta 3}(z = 0)$, computed at every time step in the LESNIC. The true surface fluxes are however systematically larger than F_s. Unlike $\tau_{\theta 3}(z = 0)$, the estimation F_s is based on the largest resolved motions and does

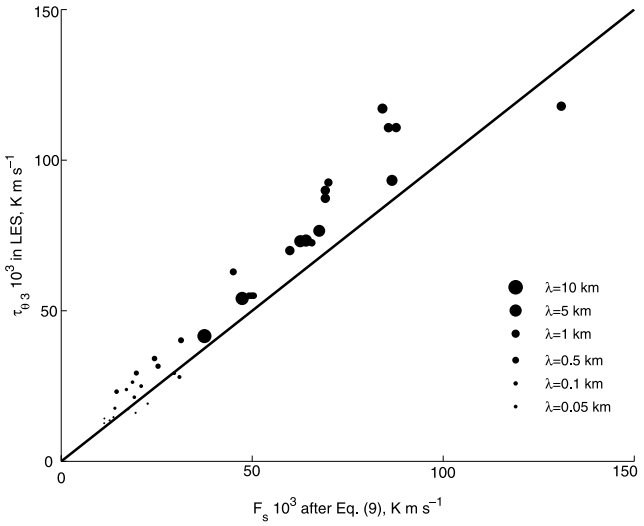

Figure 3. Comparison between the true surface temperature flux, i.e., the surface flux parameterized in the LES boundary conditions, and the estimation of the resolved-scale surface temperature flux after equation (9). The symbol size indicates the lead width in simulations.

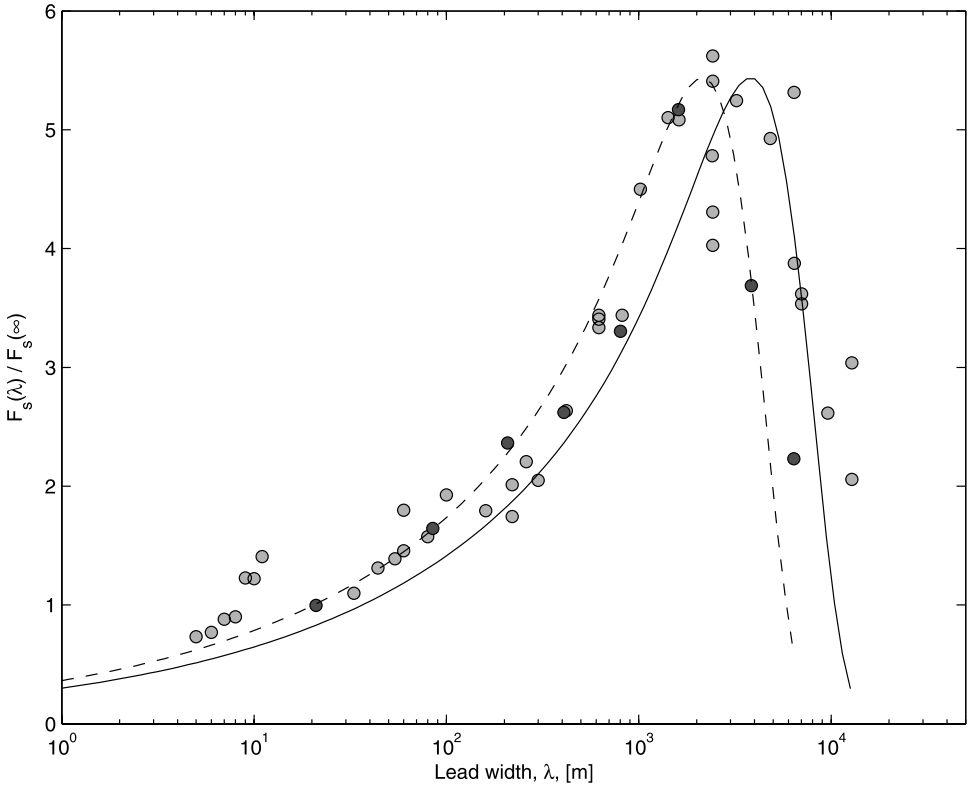

Figure 4. Ratio between the resolved-scale temperature flux $F_s(\lambda)$ and the flux $F_s(\infty)$ in the homogenous convection case. The fluxes computed after equation (9). Solid gray circles denote weakly stratified runs from Table 1 with l_{CBL} = 2.5 km; solid black circles denote strongly stratified runs from Table 2 with l_{CBL} = 1.4 km. The solid (for the weakly stratified runs) and dashed (for the strongly stratified runs) curves are an empirical fit in the form $F_s(\lambda)/F_s(\infty) = 5 \cdot (\lambda/l_{CBL})^{1/3} \cdot \exp(-(\lambda/l_{CBL} - 1)^2/4.84)$.

not include a parametric estimate of the unresolved Reynolds stress. Thus the effect of a specific subgrid parameterization on F_s should be minimal. Indeed, Figures 2 and 3 suggest that the variations in the model details and the data postprocessing account for 30% to 50% of the uncertainty in the fluxes. This is much less than the flux amplification shown in Figure 4 for two sets of the LES runs.

3.2. Resolved Surface Temperature Flux and Convective Layer Depth Sensitivities

[17] The resolved quantities in the LES are sensitive to a number of numerical parameters [e.g., *Weinbrecht and Raasch*, 2001]. Both the lead and the lead-induced circulations have to be properly resolved in simulations. This is challenging. Leads are 2 to 3 orders of magnitude smaller than the horizontal extent of the circulation. *Mori and Niino* [2002] considered different flow regimes over a heat island. Taken the gravity wave regime as the most relevant to the lead-induced circulation, one can obtain a timescale and a horizontal scale of the lead-induced circulation

$$t^{circ} = C^{circ} \cdot \left(\lambda \mathrm{Pr}_t^{1/2} \left(\beta g \Delta T_s K_H^{1/2}\right)^{-1/2}\right)^{4/5}, \qquad (10)$$
$$x^{circ} = K_H^{1/2} (\beta g \nabla_z T)^{1/2} t^{3/2},$$

where K_H is the turbulent thermal diffusivity and C^{circ} is an empirical constant equal to 1.5 for LES data. The timescale gives time needed for gravity waves (circulations) from the ice edges to meet at the lead axis. After the waves have met the circulation pattern over the lead does not change. It defines time required to reach a steady state circulation. The horizontal scale gives the distance between the ice edge and the front of the outward gravity wave propagating over ice floe. It defines the horizontal extent of the circulation at any given time. So at $t = t^{circ}$ we will find $x^{circ} = \lambda/2$. Substitution of typical values Pr_t = 1, K_H = 14 m^2 s^{-1}, ΔT_s = 8 K, $\nabla_z T = 10^{-2}$ K m^{-1} and $\lambda = 10^3$ m gives $t^{circ} \sim 0.1$ hour and $x^{circ} \sim 220$ km.

[18] As these simulations suggest neither scale is particularly good. On the one hand, Figure 5 shows that the lead-induced circulation quickly equilibrates with the turbulent convection only for the narrowest leads. For the kilometer-scale leads, the circulation pattern is formed over a few tens of minutes but the circulation velocity increases over much longer, up to 4 to 5 hours, timescale. Integrations over 6 model hours seem to be sufficient to simulate steady state circulations. *Letzel and Raasch* [2003] reported development of temporal oscillations of the boundary layer properties after 3 hours of simulations with periods 1 to 3 hours. These runs are too short to investigate the oscillations. However, 12 hour simulations for run 30 (not shown) confirmed the development of oscillations after

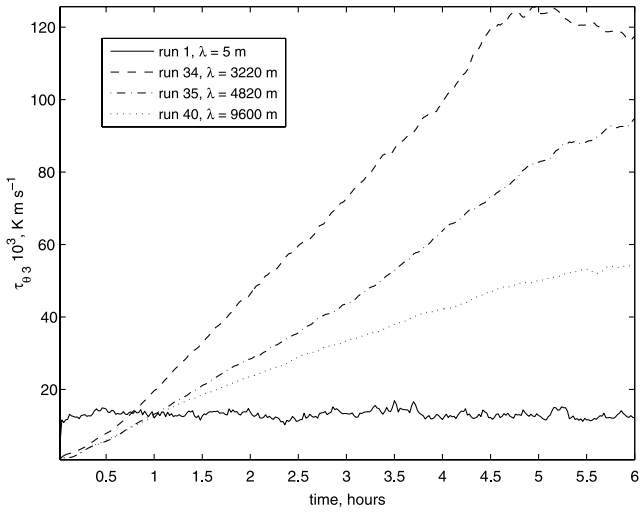

Figure 5. Temporal evolution of the parameterized surface temperature flux for runs 1 (lead width 5 m), 34 (3220 m), 35 (4820 m), and 40 (9600 m).

6 hours of simulations with the period of 5 hours and the amplitude 20% of $\langle\langle\langle \mathrm{F}_\theta\ (x,y,z,t)\ \rangle_z\rangle_{x,y}\rangle_t$.

[19] On the other hand, the sensitivity analysis below suggests that the far field circulation at 20 km and more from the ice edge provides rather small contribution into the circulation velocity and fluxes over the lead. These LES have been run in domains from 1 km to 41 km in the cross-lead direction. Periodic lateral boundary conditions, which are in use in all surveyed LES, inhibit natural development of lead-induced circulations, the main driver of the turbulent exchange for the narrow leads. Several runs allows for estimations of the sensitivity to the domain size. Table 3 presents the sensitivity computed as

$$S_D = (F_s(A) - F_s(B))/(L_x(A) - L_x(B)) \tag{11}$$

where $L_x(A)$ and L_x (B) denote the cross-lead size of the domain in runs A and B. The mean sensitivity is $S_D = 1.4 \cdot 10^{-6}$ K m s^{-1} m^{-1}. It suggests that the flux is generally larger in the larger domains with more lateral space to develop the lead-induced circulation. The 20 km domain is probably sufficiently large to saturate the circulations induced by the subkilometer-scale leads. The sensitivity for the 220 m leads is insignificant. Runs 29, 32, and 33 for the 2420 m lead revealed that S_D changes nonlinearly with the domain size. The mentioned features of S_D make the flux correction to a standard domain size unreasonable. It is worth mentioning that earlier LES [*Glendening and Burk*, 1992; *Glendening*, 1995; *Shen and Leclerc*, 1995; *Burk et al.*, 1997; *Weinbrecht and Raasch*, 2001; *Raasch and Harbusch*, 2001] were conducted in domains with horizontal dimensions less than 2.5 km. The present sensitivity analysis suggests that such a small domain should seriously damage the turbulence statistics. *Avissar and Schmidt* [1998], *Letzel and Raasch* [2003] and P05 LES were conducted in larger, up to 40 km domain. These LES are comparable with the present simulations.

[20] The mesh resolution sensitivity could be computed for runs 28 and 32 as

$$S_R = (F_s(A) - F_s(B))/(\Delta_x(A) - \Delta_x(B)) = 1.4 \cdot 10^{-3}\mathrm{K\,m\,s^{-1}m^{-1}}, \tag{12}$$

where $\Delta_x(A)$ and $\Delta_x(B)$ denote the cross-lead mesh resolution in runs A and B. As expected, the resolution refinement modestly increases F_s. The mesh resolution correction makes the data in Figure 4 only marginally less scattered.

[21] Several runs (11, 12; 14, 15; 29, 31) allow assessment of the vertical mesh resolution and the vertical size of the domain. As expected, $F_s(\lambda)$ increase with the vertical resolution refinement as a larger fraction of fluctuations is resolved. The vertical size of the domain, L_z, does not affect the fluxes until the convective boundary layer (CBL) comprises less than half of the domain depth. A deep domain is needed to simulate the outflow circulation above the CBL.

[22] Runs 21, 22 and 23 allow assessment of the LES sensitivity to perturbations in the initial state, which mimic preexisting stably stratified boundary layer (SBL) over ice. Run 22 was initialized with 0.1 K temperature fluctuations at the five lowermost levels over the lead only; run 21 was initialized with similar perturbations but over the entire domain, which initiate fluctuations in a deep SBL over ice; and run 23 was initialized with similar perturbations but limited to the five lowest layers in the entire domain, which initiate fluctuations in a shallow SBL over ice. Runs 22 and 23 are almost identical, while run 21 produced a marginally

Table 3. Sensitivity of the Surface Temperature Flux, F_s, to the Domain Size in the Cross-Lead Direction Computed After Equation (11)

Run	Domain Size, m L_x	Lead Width, m λ	$F_s \cdot 10^3$ K m s^{-1}	Sensitivity, K m s^{-1}m^{-1} $S_D \cdot 10^7$
16	20480	220	37	
17	40960	220	32	−2
29	20480	2420	105	
32	10240	2420	75	29
29	20480	2420	105	
33	40960	2420	134	14
32	10240	2420	75	
33	40960	2420	134	19
36	40960	6420	99	
37	20480	6440	72	13
41	20480	12820	38	
42	40960	12820	57	10

deeper convective layer and insignificantly, about 3%, larger $F_s(\lambda)$. Hence the preexisting shallow SBL has no effect on the lead-induced convection. The fact suggests that measurements in the preexisting SBL, usually inaccessible, are not critical to set up numerical experiments for observed cases of the lead-induced convection.

[23] Runs 29, 30 and 38, 39 allow assessment of the sensitivity to the Coriolis force. Expectedly [e.g., *Mironov et al.*, 2000], the convection over the lead is only marginally sensitive to the Coriolis force as the turbulent diffusion is dominant. The far field circulation however recovers the geostrophic balance so that the lead-induced flow becomes almost parallel to the lead axis at several kilometers from the ice edge. More detailed analysis of the far field is out of scope of this study.

3.3. Turbulent Kinetic Energy and Surface Momentum Flux

[24] The resolved-scale turbulent kinetic energy could be calculated at every grid node from resolved velocity fluctuations as $E = {}^1\!/_2(u'u' + v'v' + w'w')$. This quantity is averaged over the open water area and over h_{CBL} to obtain the mean turbulent kinetic energy $\langle E \rangle_{\lambda,z} = \langle\langle E \rangle_\lambda \rangle_z$ for every run. For consistency with the P05 presentation, the nondimensional energy is calculated using the Deardorff scaling as

$$E^n(\lambda) = \langle E(\lambda)\rangle_{\lambda,z}/w_*^2 = \langle E(\lambda)\rangle_{\lambda,z}/(\beta g F_s(\lambda) h_{CBL})^{2/3}. \quad (13)$$

The surface friction velocity, $u_*(x,y)$, is parameterized in the LES. At every surface grid node, $u_*(x,y)$ is calculated using the neutral exchange coefficient, C_{DN} . The mean friction velocity $u_* = \langle u_*(x,y)\rangle_\lambda$ is the velocity averaged over the open water area. Except for the first couple of model levels, the simulations do not demonstrate significant dependence on the parameterization of the friction velocity. This is because the largest part of the kinetic energy is carried by well-resolved eddies. Such insensitivity suggests that a more accurate estimation of the friction velocity could be obtained during the postprocessing using one of standard algorithms. I use the TOGA-COARE algorithm [*Fairall et al.*, 1996] (C. W. Fairall, personal communication to obtain the latest version of the algorithm, 2005) to obtain $u_*^{TC} = \langle u_*^{TC}(x,y)\rangle_\lambda$. The nodes, where the TOGA-COARE algorithm diverged, have been excluded from averaging procedure.

4. Results

4.1. Lead-Induced Circulation

[25] We start discussing results with two-dimensional, averaged along the lead axes, snapshots of the surface temperature flux F_s and the velocity field. Figure 6 shows F_s (shading) and velocity (vectors) in the cross-lead section for runs 1, 24, 29, 35, 38 and 41 corresponding to the lead widths 5 m, 820 m, 2420 m, 4820 m, 7020 m, and 12,820 m. Intensive turbulent exchange over the lead rapidly warms surface layer thus lowering the pressure over the lead. It is worth mentioning that the prescribed temperature difference $(T_{i,w} - T_a)$ between the ice (water) surface and the air, $T_a = \theta(z_1)$, does not necessarily create the same fluxes in the LES as in the atmosphere. In the LES, the turbulent exchange is parameterized and idealized. For instance, neither the form drag nor stability corrections have been accounted in these LES. *Beare et al.* [2006] intercomparison suggests that the flux gradient biases are not expected to be significant.

[26] The pressure difference induces familiar breeze-like circulations. Figure 7 shows snapshots, averaged in the lead direction, of the pressure anomalies in the vertical-cross-lead section. The pressure over narrow (e.g., run 29) leads gradually lowers toward the lead axis with a distinct pressure cusp at the axis due to breeze flow convergence. The pressure over wide (e.g., run 40) leads lowers at the lead edges with distinct pressure variations over the lead interior. As it is seen, convective eddies could create strong enough pressure gradients to prevent the horizontal entrainment of the cold air in the lead interior. Figure 6 visualizes resulting structural differences in the vertical-cross-lead plain. Figure 8 visualizes the differences in the horizontal plain emphasising the role of the cellular convection (run 38) in the spatial organization.

[27] Under given experimental conditions, the leads with $\lambda < 4$ km produce a single plume over open water. For such narrow leads, the convection produces pressure fluctuations, which are smaller than pressure lowering due to the thermal heterogeneity of the surface. The pressure forces the breeze to penetrate all the way to the lead axis where it joins the convective plume to create a single strong updraft. Contrary, the leads with $\lambda > 4$ km produce multiple updrafts. For such wide leads, coherent structures in the convection are fully developed. The convective velocities can counteract the mean flow up to 2.5 m s^{-1} as it is seen in Figure 6. This is in general agreement with *Avissar and Schmidt* [1998] and *Raasch and Harbusch* [2001] conclusions. So the structures significantly alter the circulation over the lead. On average, they restrict the breeze penetration to a short distance (not more than 2 km) from the lead edge. The strongest updrafts are localized close to the ice edges with much weaker updrafts over the leads.

4.2. Turbulent Temperature Flux

[28] Structural analysis has shown that the convective overturning reduces F_s. Flux reduction over wide leads creates a broad peak in $F_s(\lambda)$ function, which has been already observed in P05 simulations. Figure 4 shows the dependence $F_s(\lambda)$. These LES data and P05 LES suggest that such flux amplification over certain leads could be a universal phenomenon related to heat islands. It results from nonlinear breeze-turbulence interactions.

[29] Within the range 2 km $< \lambda <$ 5 km, $F_s(\lambda)$ is about 5 times larger than the corresponding flux, $F_s(\infty)$, in the

Figure 6. Cross-lead snapshots of the circulations (velocity vectors) and upward temperature fluxes (gray shading, values are given as $-100 \cdot \langle F_\theta(z)\rangle_\lambda$ in K m s^{-1}) averaged in the lead axis direction for runs 1, 24, 29, 35, 38, and 41 corresponding to the lead widths 5, 820, 2420, 4820, 7020, and 12,820 m with the maximum breeze velocities (the longest vectors on the plots) of 1.2, 2.3, 2.8, 2.6, and 2.4 m s^{-1}.

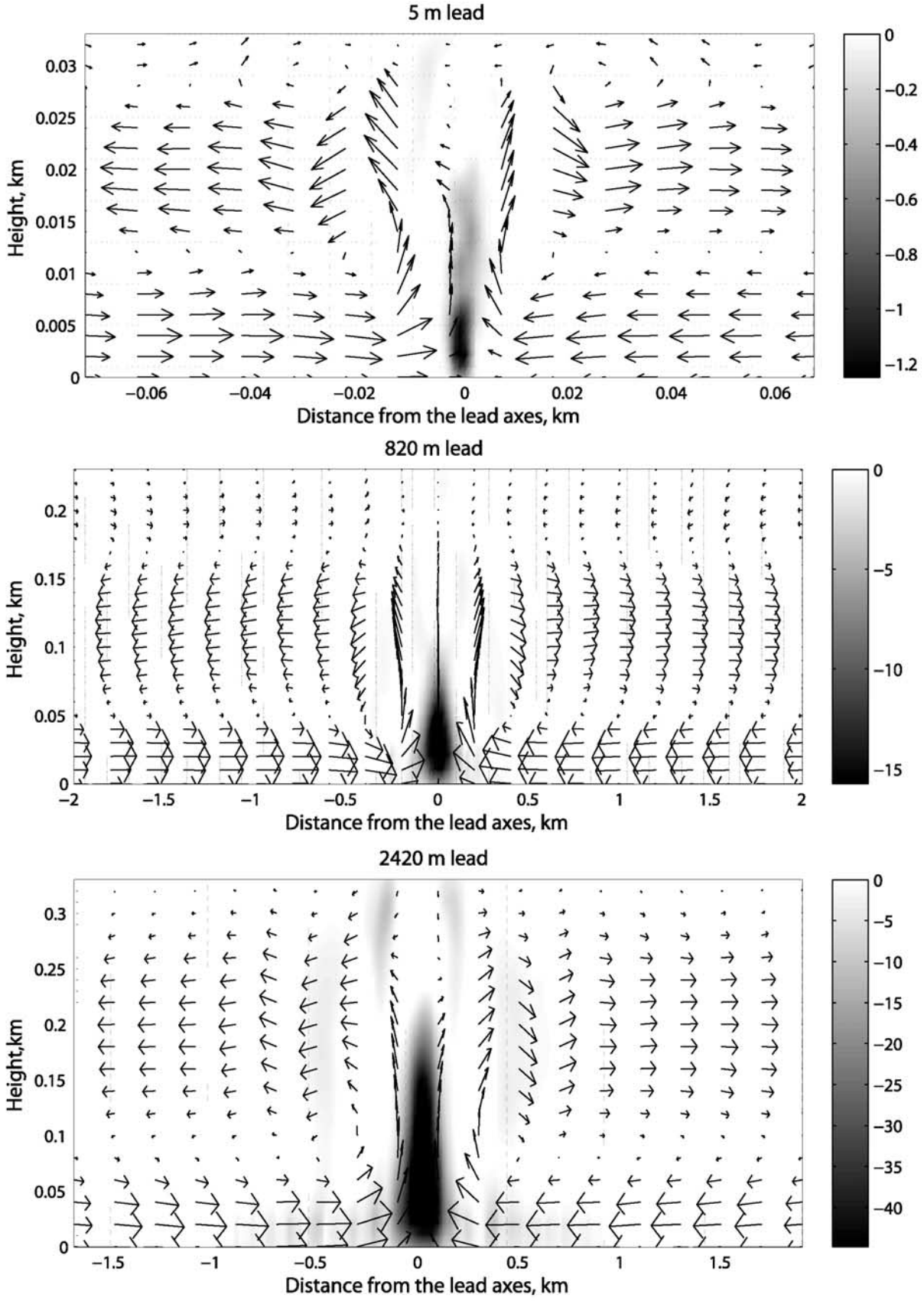
5 m lead
Height, km
0.03
0.025
0.02
0.015
0.01
0.005
0
−0.06
−0.04
−0.02
0
0.02
0.04
0.06
Distance from the lead axes, km
0
−0.2
−0.4
−0.6
−0.8
−1
−1.2
820 m lead
Height, km
0.2
0.15
0.1
0.05
0
−2
−1.5
−1
−0.5
0
0.5
1
1.5
2
Distance from the lead axes, km
0
−5
−10
−15
2420 m lead
Height,km
0.3
0.25
0.2
0.15
0.1
0.05
0
−1.5
−1
−0.5
0
0.5
1
1.5
Distance from the lead axes, km
0
−5
−10
−15
−20
−25
−30
−35
−40

Figure 6

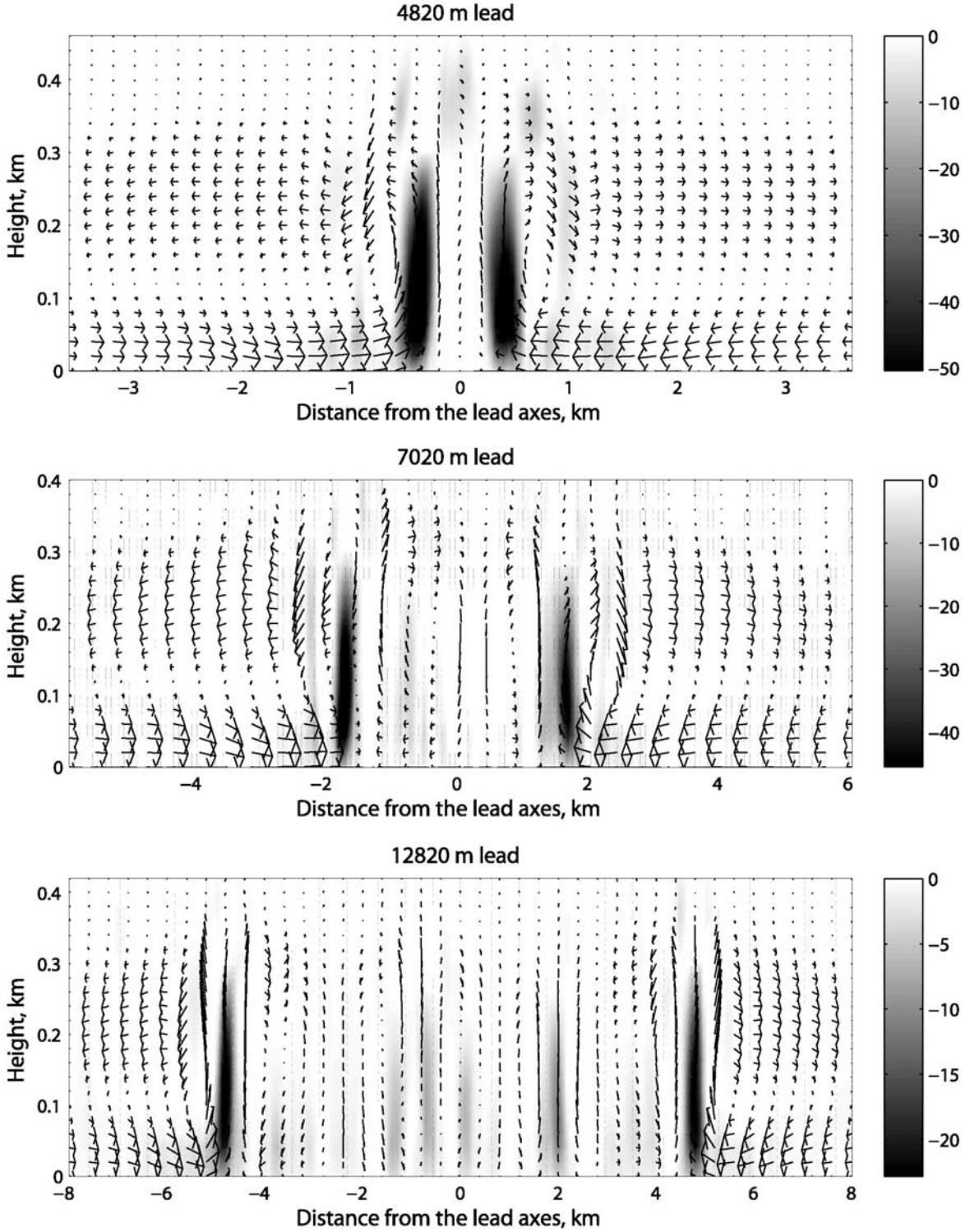

Figure 6. (continued)

homogenous convection case. Figure 4 shows that this is much larger than uncertainties due to experimental setup and model details. For $\lambda > 5$ km, the multiplume reorganization of the convection begins to reduce fluxes. The role of the self-organization becomes clearer when λ is compared with horizontal distances between updrafts, $l_{CBL} \sim 2$ km to 3 km. The distance l_{CB} e mean diameter of the convective cell, which has been determined by eye as the mean distance between the areas of the maximum upward temperature fluxes of "walls" of the convective cell (seen as the darkest shading in Figures 6 and 8). Unfortunately, there are not so many convective cells over leads in these simulations to determine l_{CBL} with some rigorous statistical algorithm. As soon as $\lambda \sim l_{CBL}$, $F_s(\lambda)$ peaks and then

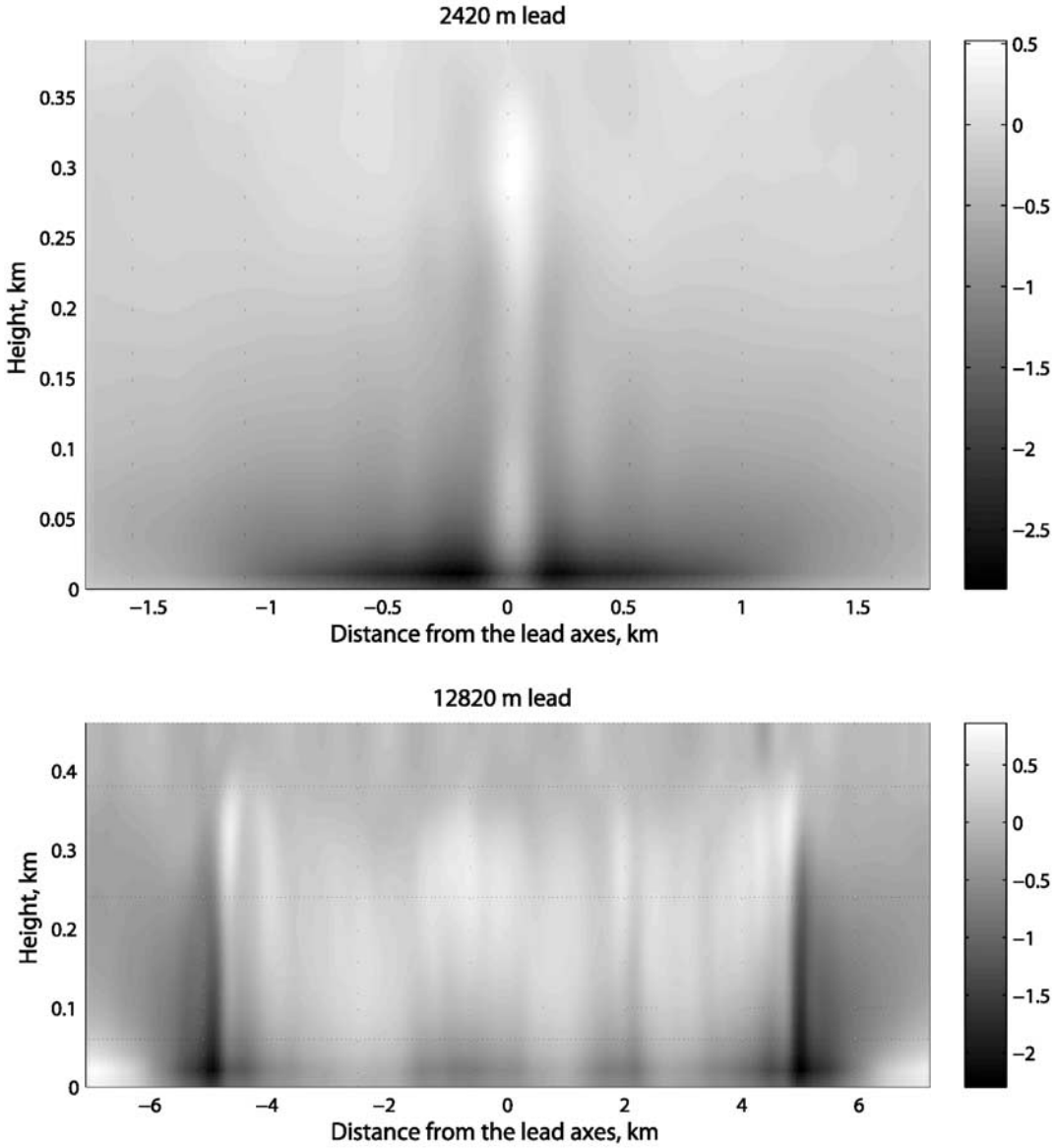

Figure 7. Vertical-cross-lead sections of the total pressure anomalies ($\langle p(x,z)\rangle_y - \langle\langle p(z)\rangle_x\rangle_y$ in $m^2\ s^{-2}$) for runs 29 and 41 corresponding to the lead widths 2420 m and 12,820 m. The light gray shading indicates higher pressure and dark gray shading indicates lower pressure. Modest pressure fluctuations within convective cells are recognizable over lead in run 41.

monotonically decays for larger λ. As the atmospheric stratification strengthen, the CBL depth and l_{CBL} decrease. The aspect ratio l_{CBL}/h_{CBL} is however preserved and equal to $\sim$8 in the present LES. This is in good agreement with the observed aspect ratio for the atmospheric convection [*Atkinson and Zhang*, 1996].

4.3. Turbulent Kinetic Energy and Momentum Flux

[30] Similar to the temperature flux, the TKE, E^n (λ), also exhibits a pronounced maximum for the kilometer-size leads. Figure 9 presents the E^n (λ) dependence in the nondimensional coordinates suggested by P05. Figure 9 reveals excellent qualitative agreement between the present and P05 simulations in spite of differences in the simulation setup and procedure. agreement suggests that the reported amplification of the temperature and momentum fluxes due to the breeze-convection interaction is not a model artifact or an artifact of idealized model setup. The amplification is a robust circulation response on the surface temperature heterogeneity. P05 have determined the nondimensional horizontal scales of the maximum flux response being in rather wide range $4 < \lambda/h_{CBL} < 9$. The present LES narrow this range to $7 < \lambda/h_{CBL} < 9$. The present LES reacts much stronger on the imposed heterogeneity. In fact, P05 studied weak surface heterogeneity due to small surface temperature differences induced by the moisture variations at an agricultural site. They obtained a relatively weak flux amplification of about 14% to 19%. Flux amplification in the present LES exceeds the factor of 4.

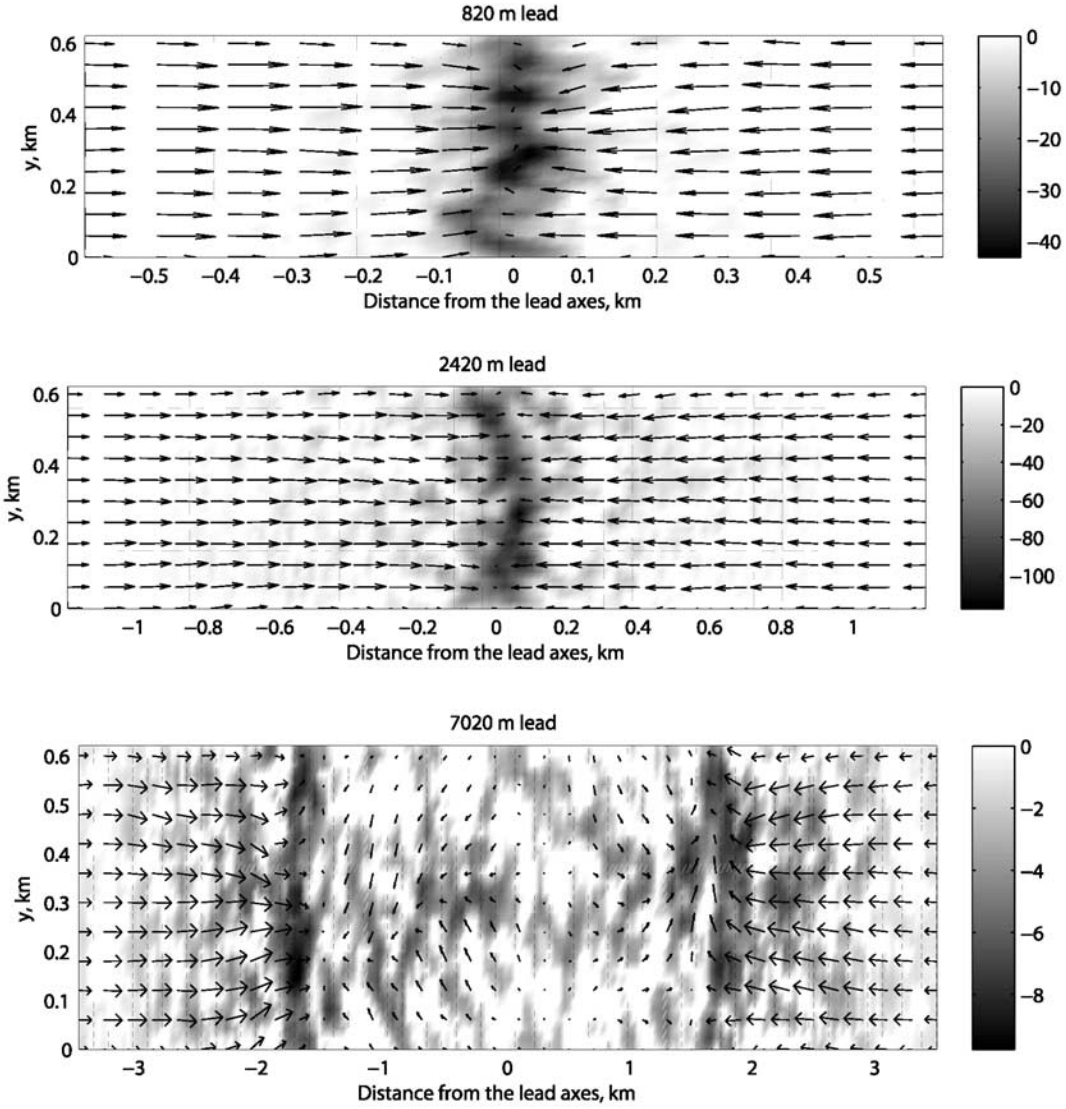

Figure 8. Snapshots of the horizontal circulation (velocity vectors) and structure of the positive temperature flux (gray shading, values are given as $-100 \cdot \langle F_\theta(x,y) \rangle_z$ in km s^{-1}) for runs 24, 29, and 38 corresponding to the lead widths 820 m, 2420 m, and 7020 m with the maximum breeze velocities (the longest vectors on the plots) of 1.2, 2.3, and 2.6 m s^{-1}. The data were averaged over levels 2 (15 m) to 5 (45 m) near the surface. At these levels the breeze-like flows are the strongest and converge toward the lead center.

[31] Enhanced turbulent exchange leads to larger mean surface wind stresses or the lead-averaged friction velocity $u_*(\lambda)$ as it is shown in Figure 10. The peak in $u_*(\lambda)$ is clearly seen in Figure 10a. The friction velocity peaks at the same lead width as $F_s(\lambda)$ does. To compare the available data with the LES, I used the TOGA-COARE algorithm [*Fairall et al.*, 1996] similar to the algorithm used in the field data processing. The TOGA-COARE algorithm, which is based on the Monin-Obukhov approach, produces significantly different value of the friction velocity, $u_*^{TC}(\lambda)$. The reason is that the approach assumes horizontally homogenous conditions. Obviously this assumption is not justified for the case of narrow leads as it has been pointed out by *Andreas and Murphy* [1986]. However, the convenience of the algorithm has pro its implementation to data processing in spite of the need for empirical corrections [*Andreas and Cash*, 1999]. Figure 10b allows for comparison with *Hartmann et al.* [1994] and *Mai et al.* [1995] data derived from REFLEX I and II campaigns. The data compares favourably with the LES.

[32] A peak could be observed in $u_*^{TC}(\lambda)$ both for the LES and observations at the ice concentrations between 50% and 80%. *Guest et al.* [1995] also reported peaking of the wind stress at the ice edge. *Mai et al.* [1995] and *Birnbaum and Lupkes* [2002] attributed the nonmonotonic wind stress behavior to a form drag due to ice edge ridges on floes. The present LES simulate neither ice ridging nor ice dynamics. Therefore the observed similarity in the friction velocity suggests that, at least partially, the stress enhancement should be attributed to the lead-induced convection.

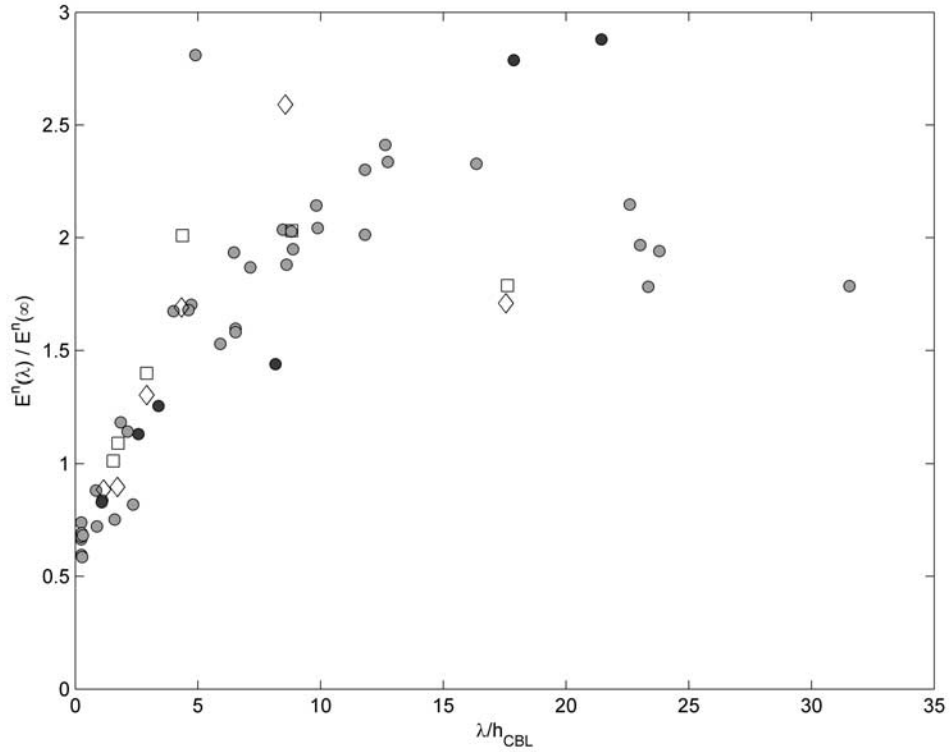

Figure 9. Ratio between convective boundary layer (CBL)-averaged, nondimensional turbulent kinetic energy (TKE), $E^n(\lambda)$, after equation (12) and the TKE, $E^n(\infty)$, in the case of homogenous convection. Runs from Table 1 (solid gray circles); runs from Table 2 (solid black circles); dry atmosphere (DP) runs from P05 (open squares); and wet atmosphere (WP) (open diamonds). P05 data are plotted as $(E^n(\lambda)/E^n(\infty))^4$ for better visibility.

4.4. Convective Layer Depth

[33] Figure 11 shows the lead-averaged convective layer depth h_{CBL} as a function of the lead width. The dependence $h_{CBL}(\lambda)$ does not have a pronounced peak. However, similarly to $F_s(\lambda)$, it is increasing for narrow leads and than levels off at values comparable with $h_{CBL}(\infty)$ in the homogeneous convection case. The behavior can be consistently explained by saturation of the internal boundary layer growth. A simple analytical model can be derived from equation (14.8) by *Arya* [2001]. Assume $\langle h_{CBL}(x) \rangle_\lambda = h_{CBL}(\lambda) \propto \langle H_i(0 < x < \lambda/2) \rangle_x$, where $H_i(x)$ is the depth of an internal convective layer. Averaging over the lead half-width gives

$$h_{CBL}(\lambda) = \frac{2}{\lambda} a_2 \int_0^{\lambda/2} \left(\frac{\Delta T_s}{\nabla_z \theta} x \right)^{1/2} dx = a_2 \frac{4}{3\sqrt{8}} \left(\frac{\Delta T_s}{\nabla_z \theta} \right)^{3/2} \lambda^{1/2} \tag{14}$$

The prefactor $a_2 = \sqrt{2A_l(1 + A_c)} = 0.154$ is a function of lateral $A_l = 0.011$ and convective $A_c = 0.125$ entrainments, which are constant fractions of $F_s(\lambda)$. This model is shown for the weekly stratified case with a solid curve in Figure 11. The proportionality between $h_{CBL}(\lambda)$ and $H_i(x)$ is incorporated into slightly changed values of A_l and A_c. One simplification is that the lateral entrainment rate, A_l , is a constant rather than a decreasing function of λ. In latter case, it would provide larger A_l at small λ and cancel $\lambda^{1/2}$-dependence in $h_{CBL}(\lambda)$ for asymptotically large λ as it is required by the LES data.

[34] *Chang and Braham* [1991] confirm the scaling $H_i(x) \propto x^{1/2}$ with measurements over the Lake Michigan. In their data, $H_i(x)$ continue to grow without limit. Contrary, the ROPEX data over Weddell Sea polynya [*Renfrew and King*, 2000] shows the remarkable saturation, $H_i(x) \rightarrow h_{CBL}(\infty)$, for fetches larger than about 5 km. Figure 11b shows the normalized averaged depth in the logarithmic coordinates. It is clear that for large leads, the scaling $\lambda^{1/2}$ works relatively good in spite of considerable data scatter and uncertainty in $h_{CBL}(\lambda)$ definition.

[35] *Mori and Niino* [2002] obtained weaker scaling $h_{CBL}(\lambda) \propto \lambda^{2/5}$ in their analytical model for an equilibrium thermal boundary layer. The scaling reads

$$h_{CBL}(\lambda) = \left(\frac{\beta g (T_w - T_a)}{\mathrm{Pr}\, K_m^2} \right)^{-1/5} \lambda^{2/5}, \tag{15}$$

where Pr = 1 is the turbulent Prandtl number and $K_m = 14\ \mathrm{m^2\ s^{-1}}$ is the turbulent eddy viscosity. The air temperature, T_a, is taken here to be equal to the temperature at the first computational level, $\theta(z_1)$. It makes $h_{CBL}(\lambda)$ slightly smaller than if it was computed with the aero-

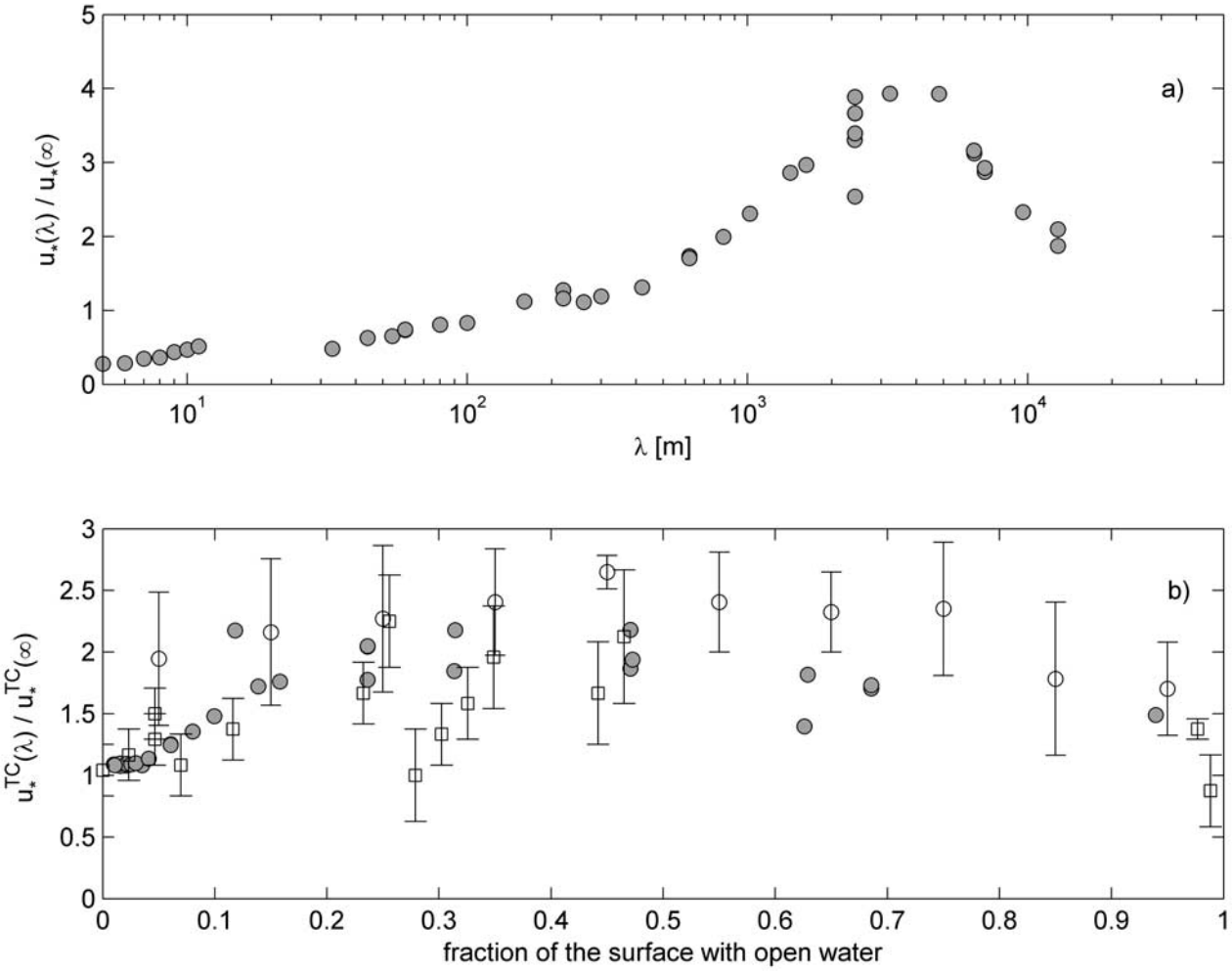

Figure 10. Dependence of the lead-averaged friction velocity, $u_*(\lambda)$, normalized by the corresponding velocity $u_*(\infty)$ in the homogenous convection case on the lead width (a). (b) Intercomparison between the LES (solid gray circles) and REFLEX data (open squares and open circles with error bars) using $u_*^{TC}(\lambda)$-friction velocity computed with the TOGA-COARE algorithm [*Fairall et al.*, 1996]. REFLEX data: open squares [*Hartmann et al.*, 1994]; open circles [*Mai et al.*, 1995].

dynamic air temperature. This model is shown for the runs from Table 1 with a dotted curve in Figure 11. It is obvious that K_m should be increased to unrealistically large values (or $T_a \rightarrow T_w$) for the model in equation (15) to agree with the data. The CBL depth in equation (15) is however not necessarily linearly proportional to our CBL depth definition.

[36] The convection over narrow leads and under strong stratification suggests slower growth. Taken over the range of leads less than 1 km wide, the scaling $h_{CBL}(\lambda) \propto \lambda^{1/3}$ agrees better with the data. Indeed, the CBL over narrow leads could be considered as a single penetrating plume but not as a fully developed boundary layer. *Zulauf and Krueger* [2003] proposed the following plume penetration height scaling

$$h_{CBL}(\lambda) = C_1 \frac{(\beta g F_\theta(\lambda) \min(\lambda, h_{CBL}(\infty)))^{1/3}}{\beta g \nabla_z \theta}. \quad (16)$$

Here the value of the constant $C_1 = 3.5$ suggests that it should account for the plume anisotropy. Zulauf and Krueger model (dashed curve in Figure 11) seems to be in good agreement with the LES data for narrow leads. Similar scaling (not shown) for a plume over a heat island was proposed by *Mori and Niino* [2002]

$$h_{CBL}(\lambda) = \left(\frac{\beta g \nabla_z \theta}{\mathrm{Pr} K_m^2}\right)^{-1/6} \lambda^{1/3}. \quad (17)$$

Summing up the results, we can conclude that the equilibrium depth of the CBL with fully developed coherent structures does not depend on the fetch. It evolves as the depth of the homogenous convection layer. The equilibrium depth of the CBL with several plumes but without self-organization of the plumes in the coherent structures evolves with the scaling $h_{CBL}(\lambda) \propto \lambda^{1/2}$, similar to the depth growth of an internal convective boundary layer. The

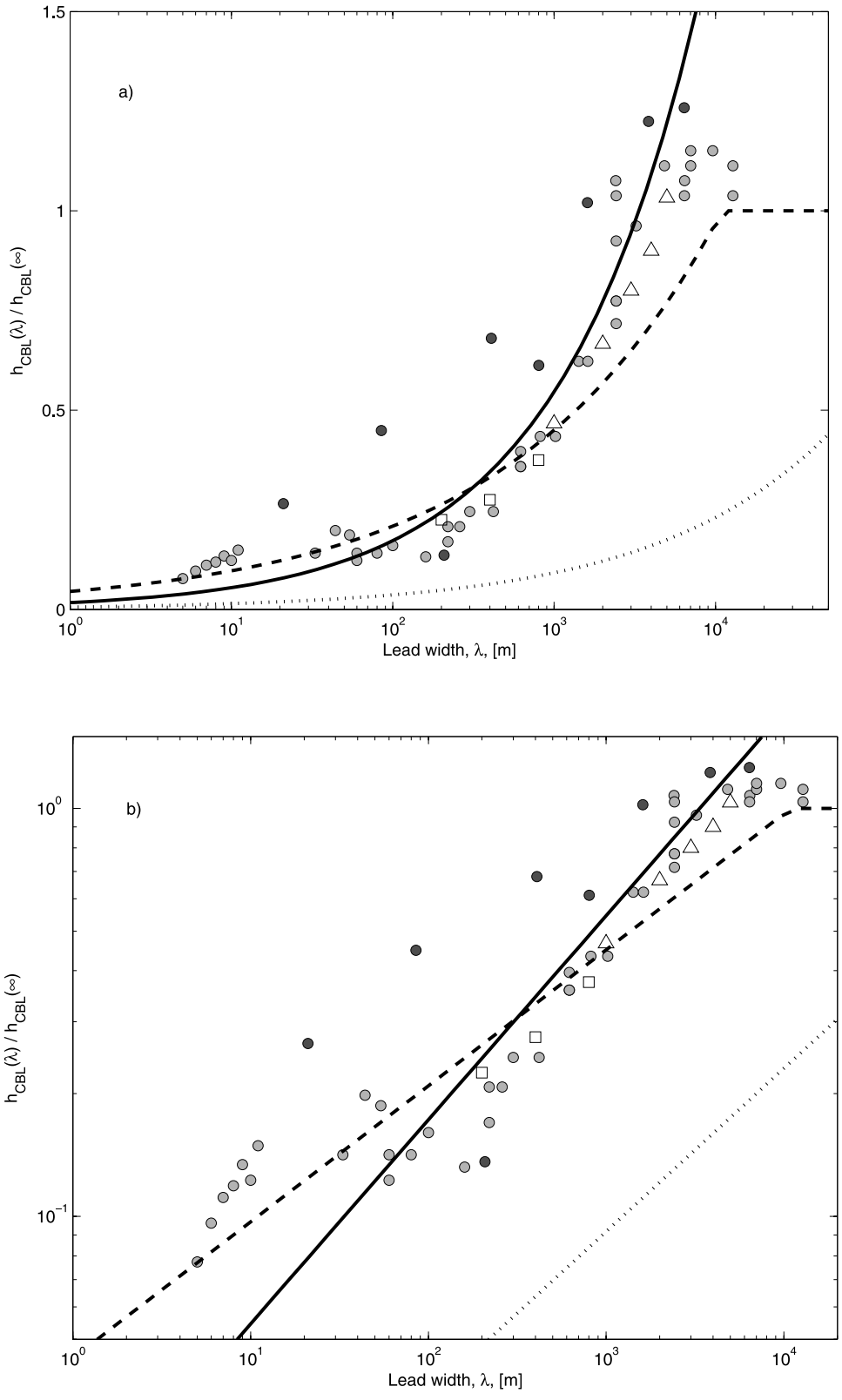

Figure 11. The mean depth of the convective boundary layer $h_{CBL}(\lambda)$ normalized by the depth $h_{CBL}(\infty)$ of the CBL in the homogenous convection case. The ordinate is linear in (a) and logarithmic in (b). Runs from Table 1 (solid grey circles); runs from Table 2 (solid black circles); *Zulauf and Krueger* [2003] simulations (open squares); and *Burk et al.* [1997] simulations (open triangles). Theoretical curves are solid: after equation (14); dotted: after equation (15); dashed: after equation (16). Theoretical curves normalized wi theoretical depth of the homogenous CBL after *Fedorovich et al.* [2004].

equilibrium depth of the CBL with a single plume evolves with the scaling $h_{CBL}(\lambda) \propto \lambda^{1/3}$.

5. Discussion on Physical Mechanisms

[37] The LES data reveals that the forced convection developing in the lead-induced breeze inflow is able to extract several times more heat per unit area of open water than the free convection over the homogeneous open water surface. Such a high efficiency of the turbulent exchange is achievable in the breeze circulation because of dominance of horizontal entrainment. Continued horizontal entrainment of cold air maintains large water-air temperature difference, and hence the effective heat loss from open water. The large temperature difference also exerts a large buoyancy force, which accelerates the circulation. However, the strong circulation may move a fluid volume out of the open water area before it has gained the maximum possible buoyancy. Since the buoyancy force, breeze velocity and the turbulent heat exchange are related nonlinearly, air in the outflow over narrow leads could be significantly underheated.

[38] The reader may notice that buoyancy force in a very high Reynolds flow should immediately lead to exponential growth of perturbations and destabilization of the flow. The breeze-like circulation in Figure 6 should break down to large eddies, which would finally produce the energy cascade to smaller and smaller eddies. Simulations show that the breeze does not break until linearly growing coherent structures develop over wider leads. Recently *Paparella and Young* [2002] have proved a nonturbulence theorem for the horizontal convection. It states that the breeze-like circulation in inviscid fluid is unconditionally stable with respect to small perturbations for moderate Rayleigh numbers *Ra*. However, the instability develops for larger *Ra*. The critical *Ra* is about $4 \cdot 10^6$. This study gives the following numbers: the turbulent Pr = 1; the heat source to the circulation depth aspect ratio $A = \lambda/(2h_{CBL}) \sim 3$; the water-air temperature difference at the surface $(T_w - T_a) = 8$ K; the turbulent eddy viscosity $K_m = 14$ m^2 s^{-1}. The numbers allows estimation of the maximal lead width with the stable breeze-like circulation as

$$\lambda_{\max} = A\left(\frac{RaK_m^2}{\beta g(T_w - T_a)}\right)^{1/3} = 4.3\,\mathrm{km} \qquad (18)$$

This estimation is in excellent agreement with the simulation analysis. The breeze destabilizes and breaks down to convective eddies organized in a cell pattern for $\lambda > \lambda_{\max}$. Since data from Table 2 represent the convection developing against stronger stratification, their mean $K_m = 6$ m^2 s^{-1} is smaller, and so their critical lead width is $\lambda_{\max} = 2.4$ km. This is again in agreement with simulations.

[39] In the steady state regime, the breeze velocity adjusts to the heat exchange rate in the surface layer so that further acceleration would result in shorter time spent by a fluid volume over the warm surface and hence in a smaller buoyancy gain. Simulations show that efficiency of the heat exchange begins to decrease for $\lambda > \lambda_{\max}$. Wider leads comprise naturally developing convective cells seen in Figure 6 and Figure 8 for run 38. Physically, the transition occurs when pre gradient induced by the cells becomes comparable with the horizontal pressure gradient induced by air-water temperature difference. The breeze circulation due to the static temperature gradients was obtained in analytical [*Dalu and Pielke*, 1989] and scaling [*Mori and Niino*, 2002] studies. The known theories of self-organized convection [e.g., *Elperin et al.*, 2006; *Manneville*, 2006] do not provide closed analytical or scaling description of the phenomenon. In particular, the aspect ratio $a_{CBL} = l_{CBL}/h_{CBL}$ of horizontal l_{CBL} to vertical h_{CBL} scales of the cells is an external parameter in those theories. The simulations show that $F_s(\lambda)$ reaches its maximum value at $\lambda/h_{CBL} \sim a_{CBL}$. This observation suggests that a_{CBL} could be a key parameter for assessment of the heat transport from leads and other sort of heat islands. Unfortunately, reviewed literature gives very uncertain margins for the possible aspect ratio in the atmospheric convection. It ranges in an interval $1 < a_{CBL} < 100$ with the most cited interval $4 < a_{CBL} < 10$ [*Atkinson and Zhang*, 1996; *Manneville*, 2006] without clear indication of its dependence on external parameters. Probably, as recently *Raasch and Schröter* [2002], *de Roode et al.* [2004], and *Schröter et al.* [2005] have suggested, diabatic heat sources could affect the aspect ratio significantly. The present study gives $6 < a_{CBL} < 8$ in the free convection.

[40] At scales $\lambda/h_{CBL} > 1.2\ a_{CBL}$, the structures begin to affect lead-induced convection considerably. The structures entrain cool air in the vertical direction as there is no temperature difference over the open water surface. Since the free atmosphere is stably stratified, the vertical entrainment consumes about 50% of the kinetic energy available for the heat transport in the case without the structures. In addition, downdraughts restrict the heat exchange to the surface layer over large areas. It leads to rise of the surface air temperature and decreases $F_s(\lambda)$ even more.

6. Conclusions

[41] This study presented a new set of 52 large-eddy simulations of lead-induced atmospheric convection over idealized leads of different widths. More generally, one may view these simulations as LES of the self-induced circulation over any heat island created by the surface temperature difference. The simulations have been done with the new code LESNIC in large domains. The limited sensitivity analysis, presented in this study, disclosed the importance of adequate horizontal and vertical size of the LES domain, which is required for undisturbed development of the breeze-like circulations, the main driver of the turbulent exchange over leads. The circulations are typically 2 to 3 orders of magnitude larger than the leads. Hence even narrow lead simulations are computationally demanding. They require a 10 km or more horizontal and hundreds meters vertical domain sizes. The domain size, sensitivity analysis and longer time of integration distinguish these simulations from the earlier model studies.Unlike earlier studies, this work focuses on dependences on the lead width. The main discovery is that the turbulent exchange peaks for certain lead widths and then reduces again to the level characterizing the turbulent exchange in the case of homogenous convection. The peak turbulent temperature flux was found to be almost 5 times larger than the corresponding flux in the homogenous convection case.

The peak turbulent kinetic energy and the peak surface stress were almost 4 times larger. Although there is no direct observational data to support this modeling study, data from independent modeling study by *Patton et al.* [2005] and indirect data from REFLEX field campaign [*Hartmann et al.*, 1994; *Mai et al.*, 1995] seem to agree, at least qualitatively, with the found nonmonotonic behavior of the fluxes.

[42] The leads, which induce the maximum fluxes, have the widths between 1 km and 5 km. The earlier studies have been focused on very narrow leads, $\lambda < 200$ m. For such leads, fluxes do not demonstrate clear amplification. Earlier analytical models, based only on the analysis of narrow leads, incorrectly assigned the monotonic flux reduction for the whole range of observed lead widths. This study showed that extrapolation of the observed turbulence exchange over narrow leads onto wider, kilometer-scale leads is not justified. One possible reason is the observed change in the turbulence self-organization occurring with development of coherent structures, namely, the convective cells. The pressure anomalies in the fully developed structures could be comparable in magnitude with the pressure anomaly due to surface thermal heterogeneity. Thus the structures raise pressure over the central part of the leads limiting the horizontal entrainment of the cold air to 1 km to 2 km from the ice edge. To preserve continuity, the energy consuming vertical entrainment over the lead central area develops. This development likely results in the observed flux reduction.

[43] Although the self-organization of the turbulent convection is known for hundred years [*Manneville*, 2006], there is no consistent theory to predict the horizontal scales of the convective cells. The present simulations give the visual horizontal cell scale of about 3 km and so the aspect ratio $6 < a_{CBL} = l_{CBL}/h_{CBL} < 8$. As soon as $\lambda/h_{CBL} \sim 1.2\, a_{CBL}$, the turbulent exchange peaks. In these estimations, the mean CBL depth h_{CBL} was found empirically. Its dependence on external parameters is an open problem. The existing analytical approximations fail to predict h_{CBL} over the whole range of possible lead widths.

[44] The study calls for theoretical understanding and development of better analytical models. This is important as kilometer-size leads are often observed in the Arctic Ocean ice cover and may have considerable impact on the Arctic energy budget and Arctic modeling.

[45] **Acknowledgments.** This study was supported by the Norwegian research project MACESIZ (Marine Climate and Ecosystems in the Seasonal Ice Zone), contract 155945/700. Useful discussions with S. Zilitinkevich, S. Larsen and T. Soomere were supported by the Nordplus NABO networking project FI-51.

References

Alam, A., and J. Curry (1997), Determination of surface turbulent fluxes over leads in Arctic sea ice, *J. Geophys. Res.*, *102*(C2), 3331–3343.

Andreas, E. L., and B. A. Cash (1999), Convective heat transfer over wintertime leads and polynyas, *J. Geophys. Res.*, *104*(C11), 25,721–25,734.

Andreas, E. L., and B. Murphy (1986), Bulk transfer coefficients for heat and momentum over leads and polynyas, *J. Phys. Oceanogr.*, *16*, 1875–1883.

Arya, S. P. (2001), *Introduction to Micrometeorology*, *Int. Geophys. Ser.*, vol. 79, 420 pp., Elsevier, New York.

Atkinson, B. W., and J. W. Zhang (1996), Mesoscale shallow convection in the atmosphere, *Rev. Geophys.*, *34*, 403–431.

Avissar, R., and T. Schmidt (1998), An evaluation of the scale at which ground-surface heat flux patchiness affects the convective boundary layer using a large-eddy simulation model, *J. Atmos. Sci.*, *55*(16), 2666–2689.

Barry, R. G., M. W. Miles, R. C. Cianflone, G. Scharfen, and R. C. Schell (1989), Characteristics of Arctic sea ice from remote-sensing data and their relationship to atmospheric processes, *Ann. Glaciol.*, *12*, 9–15.

Beare, R. J., et al. (2006), An intercomparison of large-eddy simulations of the stable boundary layer, *Boundary Layer Meteorol.*, *118*(2), 247–272.

Birnbaum, G., and C. Lupkes (2002), A new parameterization of surface drag in the marginal sea ice zone, *Tellus, Ser. A*, *54*, 107–123.

Burk, S. D., R. W. Fett, and R. E. Englebretson (1997), Numerical simulation of cloud plumes emanating from Arctic leads, *J. Geophys. Res.*, *102*(D14), 16,529–16,544.

Chang, S. S., and R. R. Braham (1991), Observational study of a convective internal boundary layer over Lake Michigan, *J. Atmos. Sci.*, *48*(20), 2265–2279.

Dalu, G. A., and R. A. Pielke (1989), An analytical study of the sea breeze, *J. Atmos. Sci.*, *46*(12), 1815–1825.

de Roode, S., P. Duynkerke, and H. Jonker (2004), Large eddy simulation of atmospheric boundary layers: How large is large enough?, *J. Atmos. Sci.*, *61*, 403–421.

Eisen, O., and C. Kottmeier (2000), On the importance of leads in sea ice to the energy balance and ice formation in the Weddell Sea, *J. Geophys. Res.*, *105*(C6), 14,045–14,060.

Elperin, T., N. Kleeorin, I. Rogachevskii, and S. S. Zilitinkevich (2006), Formation of large-scale semi-organized structures in turbulent convection, *Boundary Layer Meteorol.*, *119*, 449–472.

Esau, I. N. (2004), Simulation of Ekman boundary layers by large eddy model with dynamic mixed subfilter closure, *Environ. Fluid Mech.*, *4*(3), 273–303.

Esau, I., and S. S. Zilitinkevich (2006), Universal dependences between turbulent and mean flow parameters in stably and neutrally stratified planetary boundary layers, *Nonlinear Processes Geophys.*, *13*, 122–144.

Fairall, C. W., E. F. Bradley, D. P. Rogers, J. B. Edson, and G. S. Young (1996), Bulk parameterization of air-sea fluxes for TOGA COARE, *J. Geophys. Res.*, *101*, 3747–3767.

Fedorovich, E., R. Conzemius, I. Esau, F. K. Chow, D. C. Lewellen, C.-H. Moeng, D. Pino, P. P. Sullivan, and J. Vila (2004), Entrainment into sheared convective boundary layers as predicted by different large eddy simulation codes, in *16th Symposium on Boundary Layers and Turbulence*, paper P4.7, pp. 1–14, Am. Meteorol. Soc., Boston. (Available at http://ams.confex.com/ams/BLTAIRSE/techprogram/paper_78656.htm)

Glendening, J. W. (1995), Horizontally integrated atmospheric heat flux from an Arctic lead, *J. Geophys. Res.*, *100*(C3), 4613–4620.

Glendening, J. W., and S. D. Burk (1992), Turbulent transport from an Arctic lead: A large-eddy simulation, *Boundary Layer Meteorol.*, *59*, 315–339.

Guest, P. S., K. L. Davidson, J. E. Overland, and P. A. Frederickson (1995), Atmosphere-ocean interactions in the marginal ice zones of the Nordic seas, in *Arctic Oceanography: Marginal Ice Zones and Continental Shelves Coastal and Estuarine Studies*, vol. 49, edited by W. O. Smith and J. Grebmeier, pp. 51–95, AGU, Washington, D. C.

Hartmann, J., C. Kottmeier, C. Wamser, and E. Augstein (1994), Aircraft measured atmospheric momentum, heat and radiation fluxes over Arctic sea ice, in *The Polar Oceans and Their Role in Shaping the Global Environment*, vol. 85, *Geophys. Monogr. Ser.*, edited by O. M. Johannessen, R. D. Muench, and J. E. Overland, pp. 443–454, AGU, Washington, D. C.

Inoue, J., M. Kawashima, Y. Fujiyoshi, and M. Wakatsuchi (2005), Aircraft observations of air-mass modification over the sea of Okhotsk during sea-ice growth, *Boundary Layer Meteorol.*, *117*, 111–129.

Kleissl, J., M. B. Parlange, and C. Meneveau (2003), Field experimental study of dynamic Smagorinsky models in the atmospheric surface layer, *J. Atmos. Sci.*, *61*, 2296–2307.

Kondo, J., O. Konechika, and N. Yasuda (1978), Heat and momentum transfer under strong stability in the atmospheric surface layer, *J. Atmos. Sci.*, *35*, 1012–1021.

Leslie, D. C., and G. L. Quarini (1979), The application of turbulence theory to the formulation of subgrid modelling procedures, *J. Fluid Mech.*, *91*, 65–91.

Letzel, M. O., and S. Raasch (2003), Large eddy simulation of thermally induced oscillations in the convective boundary layer, *J. Atmos. Sci.*, *60*(18), 2328–2341.

Lindsay, R. W., and D. A. Rothrock (1995), Arctic sea ice leads from advanced very high resolution radiometer images, *J. Geophys. Res.*, *100*(C3), 4533–4544.

Mai, S., C. Wamser, and C. Koltmeier (1995), Geometric and aerodynamic roughness of sea ice, *Boundary Layer Meteorol.*, *77*(3–4), 233–248.

Makshtas, A. P. (1991), *The Heat Budget of Arctic Ice in the Winter*, 77 pp., Int. Glaciol. Soc., Cambridge, U. K.

Manneville, P. (2006), Rayleigh–Benard convection: Thirty years of experimental, theoretical, and modeling work, in *Dynamics of Spatio-Temporal Cellular Structures: Henri Bénard Centenary Review*, *Springer Tracts in Modern Phys.*, vol. 207, edited by I. Mutabazi et al., pp. 41–60, Springer, New York.

Maslanik, J., and J. Key (1995), On treatments of fetch and stability sensitivity in large-area estimates of sensible heat flux over sea ice, *J. Geophys. Res.*, *100*(C3), 4573–4584.

Miles, M. W., and R. G. Barry (1998), A 5-year satellite climatology of winter sea ice leads in the western Arctic, *J. Geophys. Res.*, *103*(C10), 21,723–21,734.

Mironov, D. V., V. M. Gryanik, C. H. Moeng, D. J. Olbers, and T. Warncke (2000), Vertical turbulence structure and second moment budgets in convection with rotation: A large eddy simulation study, *Q. J. R. Meteorol. Soc.*, *126*, 477–515.

Mori, A., and H. Niino (2002), Time evolution of non-linear horizontal convection: Its flow regimes and self-similar solutions, *J. Atmos. Sci.*, *59*, 1841–1856.

Paluch, I. R., D. H. Lenschow, and Q. Wang (1997), The Arctic boundary layer in the fall season over open and frozen sea, *J. Geophys. Res.*, *102*(D22), 25,955–25,971.

Paparella, F., and W. R. Young (2002), Horizontal convection is non-turbulent, *J. Fluid Mech.*, *466*, 205–214.

Patton, E. G., P. P. Sullivan, and C.-H. Moeng (2005), Influence of idealized heterogeneity on wet and dry planetary boundary layers coupled to the land surface, *J. Atmos. Sci.*, *62*, 2078–2097.

Raasch, S., and G. Harbusch (2001), An analysis of secondary circulations and their effects caused by small-scale surface inhomogeneities using large-eddy simulation, *Boundary Layer Meteorol.*, *101*, 31–59.

Raasch, S., and M. Schröter (2002), Broadening of convective cells during cold air outbreaks: A numerical study using a parallelized large-eddy simulation model, in *NIC Symposium 2001*, *John von Neumann Inst. for Comp. Ser.*, vol. 9, pp. 433–441, John von Neumann Inst. for Comp. Ser., Jülich, Germany.

Renfrew, I. A., and J. C. King (2000), A simple model of the convective internal boundary layer and its application to surface heat flux estimates within polynyas, *Boundary Layer Meteorol.*, *94*, 335–356.

Ruffieux, D., et al. (1995), Ice pack and lead surface energy budgets during LEADEX 1992, *J. Geophys. Res.*, *100*(C3), 4593–4612.

Schröter, M., S. Raasch, and H. Jansen (2005), Cell broadening revisited: Results from high-resolution large-eddy simulations of cold air outbreaks, *J. Atmos. Sci.*, *62*, 2023–2032.

Serreze, M. C., J. A. Maslanik, M. C. Rehder, R. C. Schnell, J. D. Kahl, and E. L. Andreas (1992), Theoretical heights of buoyant convection above open leads in the winter Arctic pack ice cover, *J. Geophys. Res.*, *97*, 9411–9422.

Shen, S., and M. Y. Leclerc (1995), How large must surface inhomogeneities be before they influence the convective boundary layer structure?: A case study, *Q. J. R. Meteorol. Soc.*, *121*, 1209–1228.

Siebesma, A. P., et al. (2003), A large-eddy simulation study of shallow cumulus convection, *J. Atmos. Sci.*, *60*, 1201–1219.

Sullivan, P. P., T. W. Horst, D. H. Lenschow, C.-H. Moeng, and J. C. Weil (2003), Structure of subfilter-scale fluxes in the atmospheric surface layer with application to large eddy simulation modelling, *J. Fluid Mech.*, *482*, 101–139.

Uttal, T., et al. (2002), The surface heat budget of the Arctic, *Bull. Am. Meteorol. Soc.*, *83*, 255–276.

Vreman, A. W., B. J. Geurts, and J. G. M. Kuerten (1994), On the formulation of the dynamic mixed subgrid-scale model, *Phys. Fluids*, *6*, 4057–4059.

Walter, B., J. Overland, and P. Turet (1995), A comparison of satellite-derived and aircraft-measured surface sensible heat fluxes over the Beaufort Sea, *J. Geophys. Res.*, *100*, 4585–4591.

Weinbrecht, S., and S. Raasch (2001), High-resolution simulations of the turbulent flow in the vicinity of an Arctic lead, *J. Geophys. Res.*, *106*, 1–12.

Zilitinkevich, S. S., et al. (2006), The influence of large convective eddies on the surface layer turbulence, *Q. J. R. Meteorol. Soc.*, *132*, 1423–1456.

Zulauf, M. A., and S. K. Krueger (2003), Two-dimensional numerical simulations of Arctic leads: Plume penetration height, *J. Geophys. Res.*, *108*(C2), 8050, doi:10.1029/2000JC000495.

I. N. Esau, Nansen Environmental and Remote Sensing Center, Thormohlensgt. 47, 5006 Bergen, Norway. (igor.ezau@nersc.no)